Fluctuations of elastic interfaces in fluids: Theory, lattice-Boltzmann model, and simulation

Davide Stelitano
Department of Physics, Massachusetts Institute of Technology, Cambridge, Massachusetts 02139

Daniel H. Rothman
Department of Earth, Atmospheric and Planetary Sciences, Massachusetts Institute of Technology, Cambridge, Massachusetts 02139

(Received 13 June 2000)

We study the dynamics of elastic interfaces—membranes—immersed in thermally excited fluids. The work contains three components: the development of a numerical method, a purely theoretical approach, and numerical simulation. In developing a numerical method, we first discuss the dynamical coupling between the interface and the surrounding fluids. An argument is then presented that generalizes the single-relaxation-time lattice-Boltzmann method for the simulation of hydrodynamic interfaces to include the elastic properties of the boundary. The implementation of this method is outlined and it is tested by simulating the static behavior of spherical bubbles and the dynamics of bending waves. By means of the fluctuation-dissipation theorem we recover analytically the equilibrium frequency power spectrum of thermally fluctuating membranes and the correlation function of the excitations. Also, the nonequilibrium scaling properties of the membrane roughening are deduced, leading us to formulate a scaling law describing the interface growth, $W^2(L,t) = L^3 g(t/L^{5/2})$, where W, L, and t are the width of the interface, the linear size of the system, and the time, respectively, and g is a scaling function. Finally, the phenomenology of thermally fluctuating membranes is simulated and the frequency power spectrum is recovered, confirming the decay of the correlation function of the fluctuations. As a further numerical study of fluctuating elastic interfaces, the nonequilibrium regime is reproduced by initializing the system as an interface immersed in thermally preexcited fluids.

PACS number(s): 61.20.Ja

I. INTRODUCTION

Elastic interfaces in fluids, such as biological membranes, have spurred a strong interest in recent years not only because of their practical importance, but also because of the intriguing complexity of their phenomenology. Many aspects of this rich subject have been studied from different approaches. Since temperature and its effects play a primary role in natural phenomena, thermal fluctuations of fluid, hexatic, nematic, and polymerized membranes have been theoretically discussed in a number of works [1–6]. Also, due to their relevance to mechanical and chemical interactions in biological systems, shape transformations and fluctuating topologies of elastic interfaces immersed in fluids with, in many cases, shear flows have been thoroughly studied [7–12]. Crystalline membranes, also known as polymerized or tethered membranes, are, in particular, a fascinating subject with important concrete realizations in nature, such as the cytoskeleton of mammalian erythrocytes (red blood cells) [13,14]. Among the systems that can be physically realized in a laboratory, inorganic crystalline membranes were examined in [15,16]. On the other hand, theoretical work on tethered membranes has proved successful in addressing the crumpling transition [17–21]. Other theoretical results on finite-size effects in fluid membranes can be found in [22–24]. Furthermore, some books and reports [25–29] reviewing the statistical mechanics, thermodynamics, and geometrical structure of membranes have shed further light on the understanding of the subject.

In the present work, we focus on the physics of elastic interfaces in fluids when thermal fluctuations in the bulk generate correlated forces and subsequent excitations on the boundary. This dynamical coupling between interface and surrounding fluid is believed to be responsible for interesting phenomena, such as the flickering of erythrocytes [2] or the physical distribution of particulates inside certain lipid vescicles [30]. Because many such problems do not have a closed-form solution, numerical simulations can provide us with a valuable tool for a deeper understanding and general guidelines for designing new experiments. More generally, the ability to simulate thermally fluctuating elastic membranes in fluids allows a computational model to be effectively employed in the simulation of the biophysical systems for which the effects of a finite temperature need to be included. Computational works on fluctuating membranes have appeared rarely in the literature [11,31–33]. As an interesting example, in the work by Goetz *et al.* [31] the power spectrum of a fluctuating bilayer membrane in vacuum is obtained by molecular dynamics. Also, the reader may find in [32] an example of how a mean-field theory approach in the framework of a lattice-Boltzmann model can be effectively employed in the study of phase separation with boundaries driven by surface tension and bending stiffness. Broadly speaking, elastic forces are governed by the local curvature of the interface and their wavelengths are two to four orders of magnitude larger than molecular ones. Therefore, a major difficulty in modeling such systems is one of describing the problem at the different length and time scales of molecular and elastic interactions in a unified and consistent approach.

Our work is threefold. First, we create a numerical method for the study of fluctuating membranes. Second, we use the method to simulate phenomena associated with the coupling of the interface and the surrounding fluids. Third,

after reviewing the properties of fluctuating membranes at equilibrium, we deduce the nonequilibrium scaling law governing the interface roughening and show that our predictions are observed in simulations.

We develop a lattice-Boltzmann model. Not only does our method allow the simulation of bending waves and fluctuating membranes in fluids, but it also allows the study of more complicated physical problems, in which the interface has many distinct components and the fluids have prescribed velocity vector fields, inducing stresses on the boundary. So that our method may eventually be used to simulate complex flows in complex geometries, it is designed to produce thin interfaces, with a thickness of the order of a few (~ 3) lattice units. Accordingly, we choose not to describe the elastic boundaries by means of a slowly varying order parameter. We choose instead to represent the dynamics of interfaces with bending rigidity by means of a free energy [1,11,34], in which the location and the geometrical properties—the curvature—of the membrane appear explicitly. Thermal fluctuations are introduced in the model as a Gaussian noise in the lattice-Boltzmann equation [35,36]. The link between differential geometry and microscopic dynamics is provided by a suitable perturbation, driven by the local curvature, of the occupation numbers, similarly to a procedure already successful in the study of interfaces with surface tension [37].

This paper is organized as follows. In Sec. II we present an overview of the relevant interface and fluid dynamics. Section III focuses on the fluid-interface coupling and on how the macroscopic equations of motion for the membrane are translated into microscopic mechanical prescriptions for the occupation numbers. We thus provide the theoretical basis for building a lattice-Boltzmann computational model. Section IV reports the results of the simulation of spherical bubbles and bending waves. Also, the experimental dispersion relation is here compared to the theoretical prediction. In the following section we then discuss the theoretical description of the physics of one-dimensional fluctuating membranes coupled to thermally excited fluids. In Sec. VI we use our model to simulate fluctuating elastic interfaces and study both the nonequilibrium roughening and the stationary state. We present here the results of our computations and compare them with the theory previously outlined. Conclusions follow in Sec. VII.

II. DYNAMICAL COUPLING OF ELASTIC INTERFACES TO AN EXTERNAL FORCE

In this section we provide a theoretical motivation for the lattice-Boltzmann microscopic dynamics that constitutes the basis of our model. We recall the common expression of the free energy for elastic interfaces and apply Hamilton's variational principle to recover the macroscopic equation of motion.

The dynamics of membranes with bending or flexural rigidity ϵ and surface tension σ is assumed to be governed, for the case of a vanishing spontaneous curvature, by the free energy [1,11,34]

$$\mathcal{F}=\frac{1}{2}\epsilon\int dSH^2+\bar{\epsilon}\int dSK+\sigma\int dS, \tag{2.1}$$

where the integrations are performed over the area of a two-dimensional (2D) membrane or over the length of a 1D interface. H is the sum of the principal curvatures and K is their product (the Gaussian curvature). $\bar{\epsilon}$ is named the saddle-splay modulus and the second term in the above equation is responsible for the energy gain/loss due to a change in the interface genus, according to the Gauss-Bonnet theorem $\int dSK=2\pi\chi=4\pi(1-g)$, where χ is the Euler-Poincaré characteristic of the surface and g is its genus [38]. For the 1D interfaces studied here, this term acts as a spontaneous curvature. Since we set it to vanish, the saddle-splay term will be neglected. The dynamical coupling of the membrane with its surroundings is realized by introducing the force $\boldsymbol{F}$ per unit area or unit length exerted by the fluids on the interface. By applying Hamilton's variational principle to the free energy (2.1) and including a term for the work done by $\boldsymbol{F}$ when the membrane undergoes a configurational change [1,39,40], the following relation between $F_\perp$, the component of the force perpendicular to the interface, and the geometric properties is derived in Appendix A:

$$F_\perp=\sigma H+\epsilon H\sum\gamma_i^2-\epsilon\nabla^2 H. \tag{2.2}$$

Here the γ_i's are the principal curvatures of the $(n-1)$-dimensional hypersurface. This expression specializes to the case of a 1D membrane as

$$F_\perp=\sigma\gamma+\epsilon\gamma^3-\epsilon\frac{d^2\gamma}{ds^2}. \tag{2.3}$$

In Eq. (2.3) s is the arclength of a canonical parametrization of the interface and $\gamma(s)$ is the local curvature.

III. NUMERICAL METHOD

The lattice-Boltzmann method [37,41] that we adopt solves the incompressible Navier-Stokes equations for the fluid dynamics, namely,

$$\rho(\partial_t\mathbf{u}+\mathbf{u}\cdot\boldsymbol{\nabla}\mathbf{u})=\mu\nabla^2\mathbf{u}-\boldsymbol{\nabla}p,$$
$$\boldsymbol{\nabla}\cdot\mathbf{u}=0. \tag{3.1}$$

Here $\mathbf{u}$ is the fluid macroscopic velocity, p the local pressure, ρ the density, and μ the viscosity coefficient. We show in this section how $\mathbf{u}$, p, and ρ are expressed in terms of microscopic quantities and how the coupling between the fluid dynamics (3.1) and the interface dynamics (2.3) is realized by means of the microscopic pressure tensor.

In making the connection between the macroscopic relation (2.3) and the microscopic dynamics of our lattice-Boltzmann method, we shall follow a procedure that has been previously employed for interfaces with surface tension [37,42]. Notice first that $F_\perp$ corresponds to the local fluid pressure gap $\Delta p=p_1-p_2$ across the interface, so that one can rewrite Eq. (2.3) as

$$\Delta p(s)=\sigma\gamma(s)+\epsilon\gamma^3(s)-\epsilon\ddot{\gamma}(s), \tag{3.2}$$

where an overdot denotes the derivative with respect to the arclength. The mechanical relation [37,43] between the normal pressure and the longitudinal pressure p_t reads

$$\Delta p(s)=\gamma(s)\int_{-\infty}^{\infty}[\overline{p_n}(s)-p_t(s,y)]dy, \tag{3.3}$$

where the integration is carried out along the y direction perpendicular to the interface. The average between the pressures at either side of the membrane is $\overline{p_n}\equiv(p_1+p_2)/2=p_2+\Delta p/2$. In practice $\Delta p\ll(\overline{p_n}-p_t)<\overline{p_n}$. We therefore simply replace $\overline{p_n}(s)$ with $p_n(s)\approx p_1(s)\approx p_2(s)$ and recast Eq. (3.2) as

$$\gamma\int_{-\infty}^{\infty}[p_n-p_t]dy=\sigma\gamma+\epsilon\gamma^3-\epsilon\ddot{\gamma}. \tag{3.4}$$

In the lattice-Boltzmann method [37,41], the momentum flux tensor $\mathbf{\Pi}$ is expressed in terms of the discretized velocity distribution functions $n_i(\mathbf{x},t)$,

$$\mathbf{\Pi}(\mathbf{x},t)=\sum_i n_i(\mathbf{x},t)\mathbf{c}_i\mathbf{c}_i, \tag{3.5}$$

where $n_i(\mathbf{x},t)$ represents the positive real-valued occupation number at a given site $\mathbf{x}$ and time t with velocity $\mathbf{c}_i$. Similar expressions hold for the fluid density and velocity,

$$\rho=\sum_i n_i(\mathbf{x},t), \tag{3.6}$$

$$\rho\mathbf{u}=\sum_i n_i(\mathbf{x},t)\mathbf{c}_i. \tag{3.7}$$

In the present work, interfaces separate the two components, called ''red'' and ''blue,'' of a binary fluid. The sum of the red occupation numbers r_i and the blue ones b_i at each lattice site is preserved:

$$n_i(\mathbf{x},t)=r_i(\mathbf{x},t)+b_i(\mathbf{x},t). \tag{3.8}$$

Starting from this distinction in terms of color attributes, it is possible to build a numerical method and study miscible and immiscible fluids, and, after suitable generalizations, the physics of even more complex fluids can be discussed [37,44].

The different components of $\mathbf{\Pi}$ are related to the macroscopic pressure tensor. Let us assume, for example, that the interface is oriented parallel to the x axis in a neighborhood of a given point $(x_p,0)$. Then Π_{yy} and Π_{xx} replace p_n and p_t, respectively, in Eq. (3.4), resulting in

$$\gamma\sum_{k=-\infty}^{\infty}\sum_i n_i(x_p,k,t)(c_{iy}^2-c_{ix}^2)=\sigma\gamma+\epsilon\gamma^3-\epsilon\ddot{\gamma}, \tag{3.9}$$

where k is the discrete coordinate running along the y axis.

The microscopic dynamics governing the time evolution of the distribution functions is described by the Boltzmann equation. Lattice-Boltzmann models rely on a discretized form of it, namely [37,41,45],

$$n_i(\mathbf{x}+\mathbf{c}_i,t+1)=n_i(\mathbf{x},t)+\Delta_i[n(\mathbf{x},t)], \tag{3.10}$$

where the last term is the collision operator, which accounts for the change in the occupation numbers due to collisions at the lattice sites. For practical reasons, $\Delta_i[n(\mathbf{x},t)]$ is usually replaced by its linear expansion around the equilibrium populations $n_i^{\mathrm{eq}}(\mathbf{x},t)$ [46]

$$\Delta_i[n(\mathbf{x},t)]=\sum_j L_{ij}[n_j(\mathbf{x},t)-n_j^{\mathrm{eq}}(\mathbf{x},t)], \tag{3.11}$$

where L_{ij} is a matrix of constant coefficients. A further simplification consists in substituting L_{ij} with a diagonal operator $\lambda_B\delta_{ij}$, where λ_B is the relevant eigenvalue of the linearized Boltzmann operator, so that Eq. (3.10) simplifies in the single-relaxation-time lattice-Boltzmann model [47,48] to

$$n_i(\mathbf{x}+\mathbf{c}_i,t+1)=(1+\lambda_B)n_i(\mathbf{x},t)-\lambda_B n_i^{\mathrm{eq}}(\mathbf{x},t). \tag{3.12}$$

This expression conserves mass and momentum. Also, the populations n_i, in the absence of external forcing, converge to the equilibrium occupation numbers n_i^{eq}.

Thermal fluctuations are introduced in the model by adding a stochastic term $\Delta_i'(\mathbf{x},t)$ to the right-hand side of Eq. (3.12) such that [35]

$$\Delta_i'(\mathbf{x},t)\propto\sum_{\alpha,\beta}\sigma'_{\alpha\beta}(\mathbf{x},t)\,(c_{i\alpha}c_{i\beta}-c^2\delta_{\alpha\beta}/D). \tag{3.13}$$

Here D is the dimensionality of the lattice and the random fluctuations $\sigma'_{\alpha\beta}$ are uncorrelated in space and time [49] and sampled from a Gaussian distribution such that

$$\langle\sigma'_{\alpha\beta}(\mathbf{x},t)\sigma'_{\eta\zeta}(\mathbf{x}',t')\rangle=A\,\delta_{\mathbf{x}\mathbf{x}'}\delta_{tt'}\Big(\delta_{\alpha\eta}\delta_{\beta\zeta}+\delta_{\alpha\zeta}\delta_{\beta\eta}-\frac{2}{3}\delta_{\alpha\beta}\delta_{\eta\zeta}\Big), \tag{3.14}$$

where the variance A is related to the effective temperature T of the fluid,

$$A=2\rho\nu k_BT\lambda_B^2, \tag{3.15}$$

by means of the fluctuation-dissipation theorem [35].

In order to reproduce the desired surface tension and bending stiffness of the interface, so that the left-hand side of Eq. (3.9) does not vanish in the proximity of the boundary, one may suitably perturb the single-relaxation-time lattice-Boltzmann model by adding a term Δ_i'' to the right-hand side. Our perturbation of Eq. (3.12) reads

$$\Delta_i''\equiv(S+E\gamma^2-E\ddot{\gamma}/\gamma)|\mathbf{f}|\sum_{\alpha\beta}(c_{i\alpha}c_{i\beta}-c^2\delta_{\alpha\beta}/D)\frac{f_\alpha f_\beta}{f^2}, \tag{3.16}$$

where S and E are two adjustable parameters corresponding to the physical surface tension σ and bending rigidity ϵ, and $\mathbf{f}(\mathbf{x},t)$ is the local color gradient [37] as defined in Appendix B. In order to measure the geometric properties of the membrane—the curvature γ and its derivatives—appearing

in Eq. (3.16), we adopt an explicit procedure of localization of the different connected components of the interface. The method is described in some detail in Appendix B. There we show how, for each component, we map the boundary piecewise to polynomials, from which we extract the curvature and its derivatives. This process does not result in a significant time consumption for the whole simulation, as it is performed only once at the beginning of each time step and it is limited to the lattice sites that constitute the interface.

Expression (3.16) preserves the total mass and momentum at a given lattice site, as one can verify by recalling the identities

$$\sum_i c_{i\alpha}=0,$$

$$\sum_i c_{i\alpha}c_{i\beta}=b_m c^2\delta_{\alpha\beta}/D,$$

$$\sum_i c_{i\alpha}c_{i\beta}c_{i\gamma}=0,$$

which hold true for tensors with hypercubic symmetry. By generalizing the argument set forth in Sec. 10.2 of [37], it can be shown that the inclusion of Eq. (3.16) into the right-hand side of Eq. (3.12) generates a surface tension σ and a bending rigidity ϵ of the interface, which are related to S and E, respectively, through the linear relation

$$\frac{\sigma}{S}=\frac{\epsilon}{E}=-\frac{192\rho}{\lambda_B} \tag{3.17}$$

valid for the face-centered hypercubic (FCHC) lattice, which we shall employ throughout this work. The above result follows from replacing Eqs. (10.14) and (10.3) in [37] with our equations (3.9) and the result of the perturbation of Eq. (3.12) by Eq. (3.16) and carrying out an analysis similar to that in [37].

IV. TESTING THE MODEL

The surface tension parameter S is set to zero so that purely elastic effects can be studied. In Sec. IV A, the results for a spherical bubble surrounded by fluids on both sides are presented. In Sec. IV B, the bending wave dispersion relation is discussed by studying the damped oscillations of sinusoidal interfaces.

A. Spherical bubbles

The lattice-Boltzmann simulation is initialized as a spherical bubble of a fluid, here called ''red'' for practical purposes, immersed in a bath of ''blue'' fluid with linear dimension L much larger than the radius R of the sphere. The pressure gap Δp between the red inner part of the bubble and the outside blue sea is predicted by replacing Eq. (3.17) in Eq. (3.2), resulting in

$$\Delta p=-\frac{192\rho E}{\lambda_B}\gamma^3=-\frac{192\rho E}{\lambda_B R^3} \tag{4.1}$$

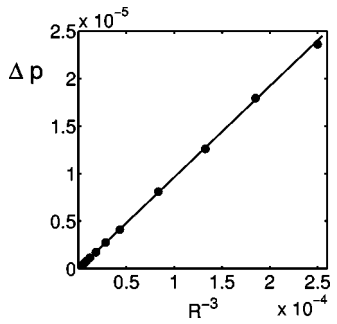

FIG. 1. Verification of the $\Delta p=\epsilon/R^3$ law for a fluid bubble immersed in an immiscible sea. The solid line is the theoretical prediction for the parameters specified in the text. The pressure gap Δp is determined from the equation of state $p(\rho)=3\rho/10$, where ρ is the fluid density. The radius R of the bubble is expressed in lattice units.

as σ is set to vanish in our experiments, $\gamma=1/R$, and $\ddot{\gamma}=0$ for a sphere. The pressure is computed by measuring the fluid density according to the equation of state (in the absence of a net momentum) [37]

$$p(\rho)=\frac{b_m\rho}{2b}, \tag{4.2}$$

where b_m is the number of velocity vectors (24 for a FCHC lattice), while $b\equiv b_m+b_r$ includes the number b_r of rest particles (in this case $b_r=16$). Simulations were performed for different bubble sizes, ranging from $R=8$ to $R=64$, with average density of 0.5 particles per lattice site, $\lambda_B=-1$, and $E=10^{-3}$. The measured values of Δp are plotted versus R^{-3} in Fig. 1. The agreement with the predicted relation $\Delta p=0.096R^{-3}$, drawn as a solid line, is very good. For bubble radii smaller than eight lattice units, discretization effects cause the measured curvature to be off more than 15%, and ultimately wrong when the radius of curvature is of the order of the interface thickness, which is about four lattice units.

B. Bending waves

While bubble pressure gaps verify the equilibrium properties of the membrane, the simulation of bending waves provides an effective tool for testing the dynamics of the fluid-interface coupling. In testing the bending wave dispersion relation, we initialize the system as a square region filled with two immiscible fluids with the same densities and viscosities. Such fluids are separated by a sinusoidal interface, whose wavelength λ is equal to the linear dimension of the box. We impose periodicity along the horizontal axis, while free-slip boundary conditions are prescribed along the vertical axis. The damped oscillations of bending waves for membranes immersed in viscous fluids have been analytically studied in the literature [50]. For the initial conditions we impose one expects the time dependence of the first normal mode to be described by

$$h_{k_1}(t)=h^0_{k_1}\cos[\mathrm{Re}(\omega)t]\,e^{-\mathrm{Im}(\omega)t}, \tag{4.3}$$

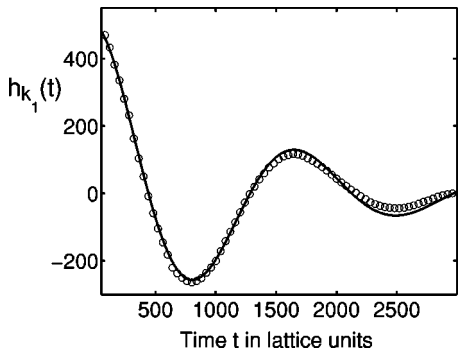

FIG. 2. The results of the lattice-Boltzmann simulation of a bending wave with wavelength $\lambda = 100$ lattice units (circles). The theoretical predictions from the normal-mode analysis, Eqs. (4.3) and (4.4), are graphed as a solid line. $h_{k_1}(t)$ is the Fourier transform in lattice units of the interface profile, corresponding to the wave number $k_1 = 2\pi/\lambda$.

where $k_1 = 2\pi/L$, with L the size of the box, and $h^0_{k_1}$ is the initial amplitude of the sinusoidal wave. The complex angular frequency ω is related to the wave number $k \equiv 2\pi/\lambda$ through the dispersion relation [2]

$$\omega^2 = \frac{\epsilon k^5}{2\rho}(1 - k/q), \qquad (4.4)$$

$$q = \sqrt{k^2 - i\omega/\nu},$$

where $\nu = \mu/\rho$ is the kinematic shear viscosity. The numerical simulation of a bending wave for a system defined by $E = 0.25$, $L = 100$, $\rho = 0.5$, $\lambda_B = -1.0$, $h^0_{k_1}/L = 0.05$ is given as an example in Fig. 2. By means of Eqs. (3.17) and (4.4) and the relation between the viscosity ν and the Boltzmann eigenvalue λ_B [37],

$$\nu = -\frac{1}{3}\left(\frac{1}{\lambda_B} + \frac{1}{2}\right). \qquad (4.5)$$

Therefore one may fully predict the behavior of the normal mode (4.3). $h_{k_1}(t)$ was computed as the Fourier transform of the experimental interface profile $h(x,t)$, recorded at each time step. Figure 2 shows the evolution of $h_{k_1}(t)$ according to Eq. (4.3) (solid line) and our numerical results (circles). By fitting the first cycle of the time evolution of $h_{k_1}(t)$ to a curve of the form (4.3) ($h^0_{k_1}$ is initially prescribed) we collected the numerical data about the complex angular frequency ω, whose real and imaginary parts correspond to the oscillation frequency and damping rate, respectively, of the bending wave. We repeated the simulation of Fig. 2 for different wavelengths, collecting the data about the damping rates $\mathrm{Im}(\omega)$ and the oscillation frequencies $\mathrm{Re}(\omega)$. In Fig. 3 we produce the experimental results together with the numerical solution of Eq. (4.4). We notice that the agreement between experimental data and theoretical predictions improves for larger systems and the relative errors reduce to few percent for wavelengths of $O(10^2)$ lattice units. The

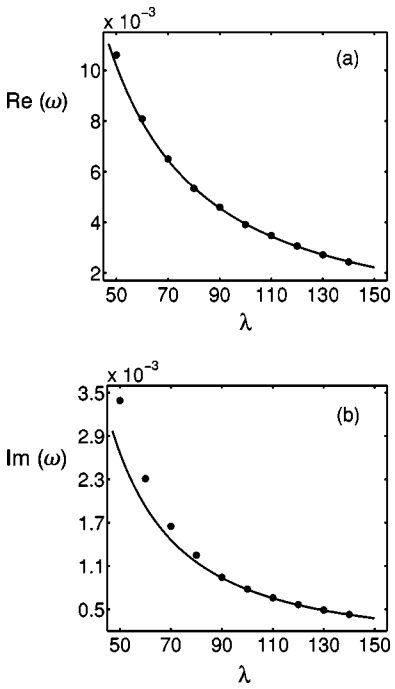

FIG. 3. (a) Oscillation frequencies collected from the simulation of bending waves with wavelengths ranging from 50 to 140 lattice units are represented with filled circles. The numerical solution of Eq. (4.4) is drawn as a solid line. (b) Damping rates for the same experiment correspond to the imaginary part of the complex frequency $\mathrm{Im}(\omega)$. The discrepancy at shorter wavelenghts is due to the damping action of the effective surface tension discussed in Sec. VI B.

relative error is here defined in terms of the theoretical and experimental time evolution of the damped wave as

$$\varepsilon(\lambda) = \sqrt{\frac{1}{\tau}\sum_{t=0}^{\tau}[1 - h_{k_1,ex}(t)/h_{k_1,th}(t)]^2}, \qquad (4.6)$$

where τ is twice the oscillation period of the bending wave. Table I reports the relative errors for different wavelengths, confirming their fast convergence toward $O(10^{-2})$ when $\lambda > 70$. The error at small wavelengths is due to a numerical artifact that manifests itself as an effective surface tension. We postpone further discussion of this subject to Sec. VI B.

TABLE I. Relative errors $\varepsilon(\lambda)$ for the sinusoidal bending waves discussed in Sec. IV B and in Fig. 3.

λ	$\varepsilon(\lambda)$
50	0.2741
60	0.1915
70	0.1262
80	0.0833
90	0.0640
100	0.0519
110	0.0428
120	0.0371
130	0.0323
140	0.0289

V. THERMAL FLUCTUATIONS OF ELASTIC INTERFACES: THEORY

We now turn to a study of fluctuating membranes. This section introduces the theoretical results relevant to our discussion. A comparison with numerical experiments will then be presented in succeeding sections. The fluctuation-dissipation theorem provides us with a unified description of the steady state and the nonequilibrium growth (roughening) of fluctuating interfaces. Emphasis is given to the frequency power spectrum, as it conveys all the relevant information about the decay of the correlation function of the fluctuations.

A. Correlation functions from the fluctuation-dissipation theorem

A detailed discussion of the fluctuation-dissipation theorem and fluctuating hydrodynamic interfaces driven by surface tension has been presented in [51,52]. Here we summarize the theoretical results for 1D interfaces with bending stiffness.

The interface height will be denoted by $h(x,t)$ and its Fourier transform in wave number space by $h_k(t)$. We also introduce the Fourier transform in time as

$$\hat{h}_k(\omega)=\frac{1}{\Theta}\int_0^{\Theta} dt\, h_k(t)\, e^{-i\omega t}, \tag{5.1}$$

where Θ is the size of the time integration domain. When $\Theta\to\infty$ the integral in Eq. (5.1) will be replaced by $(1/\Theta)\int_0^{\Theta}\to(1/2\pi)\int$.

It can be shown [52,53] that the frequency power spectrum can be written in terms of the response function $\Gamma_k(\omega)$ as

$$|\hat{h}_k(\omega)|^2=\frac{\Theta}{2\pi^2}\frac{k_BT}{\omega^2 L}\mathrm{Re}[\Gamma_k(\omega)], \tag{5.2}$$

where

$$\Gamma_k^{-1}(\omega)=\frac{2\omega\rho}{ik(1-k/q)}-\frac{\epsilon k^4}{i\omega} \tag{5.3}$$

and q is given in Eq. (4.4). The frequency power spectrum carries information about the fluctuation correlation functions. Indeed, by means of the Wiener-Khintchine relation, Eq. (5.2) can be used to show that

$$\langle h_k(t)h_k^*(0)\rangle=\frac{k_BT}{2\pi L}\int_{-\infty}^{\infty}\frac{d\omega}{\omega^2}e^{-i\omega|t|}\,\Gamma_k(\omega). \tag{5.4}$$

The integration in Eq. (5.4) can be performed in the complex ω plane by means of the contour drawn in Fig. 4, so that

$$\langle h_k(t)h_k^*(0)\rangle=\langle h_k(t)h_k^*(0)\rangle_{\mathrm{bw}}+\langle h_k(t)h_k^*(0)\rangle_{\mathrm{cut}} \tag{5.5}$$

is the sum of the contributions from the two poles (bending wave) and from the branch cut. In the case of oscillating bending waves the contribution from the two poles results in

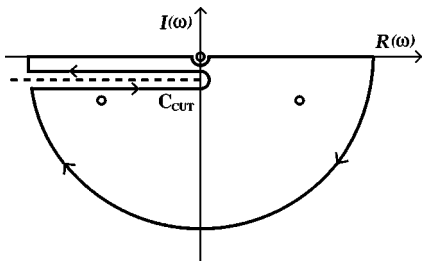

FIG. 4. Integration contour for the fluctuation correlation function (5.4). The poles in the lower half plane corresponds to the bending wave contribution, while the pole at the origin represents the steady state power spectrum.

$$\langle h_k(t)h_k^*(0)\rangle_{\mathrm{bw}}=\frac{k_BT}{\epsilon k^4 L}\left[\cos|\mathrm{Re}(\omega)t|-\left|\frac{\mathrm{Im}(\omega)}{\mathrm{Re}(\omega)}\right|\sin|\mathrm{Re}(\omega)t|\right]e^{-|\mathrm{Im}(\omega)t|}, \tag{5.6}$$

where ω as a function of k is given by the dispersion relation (4.4). Also, in the long time limit, the contribution from the branch cut reads

$$\langle h_k(t)h_k^*(0)\rangle_{\mathrm{cut}}=\frac{2k_BT\rho\nu^{1/2}}{\epsilon^2k^8L}\,\frac{e^{-k^2\nu|t|}}{|t|^{3/2}}. \tag{5.7}$$

One can show by means of the fluctuation-dissipation theorem [52] that the correlations among the fluctuating forces acting on the interface, and due to the uncorrelated thermal excitations in the bulk, have indeed the same temporal decay as Eq. (5.7). A special case is the one of $t=0$ in Eq. (5.4). The integration contour can then be closed in the upper half plane, including only the pole at $\omega=0$. As a result

$$\langle|h_k(0)|^2\rangle=\frac{k_BT}{\epsilon k^4 L} \tag{5.8}$$

represents the mean square amplitude of the kth mode [2], which can also be understood by applying the energy equipartition theorem to the free energy (2.1).

B. Interface roughening

The mean square width $W^2(L,t)$ of an interface with vanishing mean height, defined as

$$W^2(L,t)\equiv\frac{1}{L}\int_0^L dx\, h^2(x,t), \tag{5.9}$$

will be used here to describe the interface roughening. By using Parseval's relation, Eq. (5.9) can be recast as $W^2(L,t)=\Sigma_k|h_k(t)|^2$. At the steady state, the average width can be evaluated by means of Eq. (5.8),

$$W^2(L)=\frac{2k_BT}{\epsilon L}\sum_{n=1}^{\infty}\left(\frac{L}{2\pi n}\right)^4=\frac{k_BT}{720\,\epsilon}L^3, \qquad (5.10)$$

where the factor 2 accounts for the two possible orientations (for a one-dimensional interface) of the wave vectors. This result shows that at equilibrium $W/L\propto L^{1/2}$, that is, the relative width apparently increases indefinitely with the square root of the linear size of the computational box.

In reality, the argument given above and culminating with Eqs. (5.8) and (5.10) implicitly approximates the free energy $\mathcal{F}=\frac{1}{2}\epsilon\int ds\,\gamma^2$ with the more convenient expression $\mathcal{F}_{\rm ap}=\frac{1}{2}\epsilon\int dx(d^2h/dx^2)^2$. Such an approximation is certainly plausible when $\gamma\approx d^2h/dx^2$, that is, when the interface width/length ratio is small. In practice, however, when $W/L>1/2$ the local curvature is significantly different from its linearization d^2h/dx^2, and the original expression (2.1) for the free energy should be considered. Therefore Eqs. (5.8) and (5.10) hold true only for small values of W/L, while when $W/L>1/2$ nonlinear terms in the curvature and consequently in the dynamics prevent the interface width/length ratio from growing indefinitely with the size of the system. On the other hand, the lattice-Boltzmann method we are currently describing does not suffer from such a limitation. Indeed, the interface dynamics discussed in Sec. II originates in our model from the perturbation (3.16), which corresponds to the exact analytical form of the elastic force $F_{\rm el}=-\epsilon\,d^2\gamma/ds^2$ and not to its linearized approximation $F_{\rm el}\approx-\epsilon\,d^4h/dx^4$, deducible from $\mathcal{F}_{\rm ap}$. This allows us to study and simulate the dynamics of membranes in the nonlinear regime.

In order to analyze the nonequilibrium roughening of the interface, two immiscible fluids at the same temperature T are brought in contact at time $t=0$. The interface between them is initially flat. Due to the thermal fluctuations in the bulk, standing bending waves will be excited on the interface with frequencies given by the dispersion relation

$$\omega_0(k)=\sqrt{\frac{\epsilon}{2\rho}}k^{5/2}, \qquad (5.11)$$

where for simplicity we consider the inviscid limit ($\nu=0$) of Eq. (4.4). In analogy with the argument of [51,52] and by means of the fluctuation-dissipation theorem, one anticipates that the power spectrum is given by

$$\langle|h_k(t)|^2\rangle=\frac{2k_BT}{\epsilon L k^4}\sin^2[\omega_0(k)t], \qquad (5.12)$$

so that the mean square width of the interface is expected to grow as

$$W^2(L,t)=\frac{4k_BT}{\epsilon L}\sum_n\left(\frac{L}{2\pi n}\right)^4\sin^2\left[\sqrt{\frac{\epsilon}{2\rho}}\left(\frac{2\pi n}{L}\right)^{5/2}t\right], \qquad (5.13)$$

where the thermal average of W^2 is understood. The inviscid form of $W^2(L,t)$ as given by Eq. (5.13) does not hold for long times, since it does not relax to the equilibrium (5.10) as it should if the effects of a finite viscosity were taken into account. Nonetheless, the initial excitations are all in phase, as the interface starts with a flat profile, so Eq. (5.13) is a correct description of the short-time nonequilibrium growth of the interface width.

From Eqs. (5.10) and (5.13) one finds that W^2 scales according to

$$W^2(L,t)=L^3\,g(t/L^{5/2}), \qquad (5.14)$$

where for large times

$$\lim_{t\to\infty}g(t/L^{5/2})=\frac{k_BT}{720\,\epsilon}, \qquad (5.15)$$

while the short-time limit is given by

$$g(t/L^{5/2})=\frac{k_BT}{4\,\epsilon\pi^4}\sum_n\frac{1}{n^4}\sin^2\left[\sqrt{\frac{\epsilon}{2\rho}}\left(\frac{2\pi n}{L}\right)^{5/2}t\right]. \qquad (5.16)$$

One can obtain an analytical form for the above expression by approximating the summation with an integration, so that Eq. (5.13) becomes

$$W^2(t)=\frac{4k_BT}{5\,\pi(2\rho)^{3/5}\,\epsilon^{2/5}}\,t^{6/5}\int_0^{\infty}dx\,\frac{\sin^2(x)}{x^{11/5}}, \qquad (5.17)$$

where we set $x=\omega_0(k)t$. The integral evaluates to [54]

$$\int_0^{\infty}dx\,\frac{\sin^2(x)}{x^{11/5}}=\frac{5^2\,2^{1/5}}{6}\cos(2\pi/5)\,\Gamma(4/5)=1.7219\ldots \qquad (5.18)$$

and the roughening of the interface thus scales according to

$$W^2(t)=\frac{2^{3/5}\,5\cos(2\pi/5)\,\Gamma(4/5)}{3\pi}\,\frac{k_BT}{\rho^{3/5}\,\epsilon^{2/5}}\,t^{6/5}. \qquad (5.19)$$

We expect Eq. (5.19) to describe the growth of the interface until the crossover time at which equilibrium is attained. The crossover time t_c may be approximated by the time necessary for the longest-wavelength excitation to reach its maximum amplitude, that is, $t_c=\mathcal{T}/4$. If the dispersion relation (4.4) is used to estimate the period $\mathcal{T}$, we conclude that

$$t_c=\frac{\pi}{2\,\omega_0}=\frac{1}{8}\sqrt{\frac{\rho L^5}{\pi^3\epsilon}}. \qquad (5.20)$$

We shall compare the lattice-Boltzmann numerical simulations with the theoretical results of this section in the following.

VI. THERMAL FLUCTUATIONS OF ELASTIC INTERFACES: SIMULATIONS

In this section we present the results of the simulations performed using the lattice-Boltzmann method with a nine-velocity square lattice (that is, a FCHC lattice projected in

two-dimensions) [37,41]. The computational box of size $L \times L$ is filled with two immiscible fluids prethermalized to a common temperature and separated by a thin interface. The two fluids have the same densities and viscosities. We study the dynamical effects of thermal fluctuations at equilibrium and out of equilibrium, when the interface grows up to the steady state given by Eq. (5.10). The interfaces we consider are driven by the coupling with the surrounding fluids and by purely elastic forces, tuned by the bending modulus ϵ, as defined in Sec. II.

A. Steady state

The evolution of an interface of size $L=64$ was monitored for 2^{20} time steps, setting the experimental parameters to $\lambda_B=-1.5$, $\rho=0.5$, $E=0.0002$ and the variance $A=10^{-4}$. The resulting log-log plot of the frequency power spectrum is given in Fig. 5.

In order to compare the simulation data with the theory, we rewrite Eq. (5.2) in an explicit form. Let $\xi=\omega/\nu k^2$, $\omega_0=k^2\sqrt{\epsilon k/2\rho}$, $\xi_0=\omega_0/\nu k^2$. Then Eq. (5.2) can be recast as

$$|\hat{h}_k(\omega)|^2=\frac{2\rho k\nu k_B T\Theta}{\pi^2 L(\epsilon k^4)^2}\ N_{\xi_0}(\xi), \tag{6.1}$$

where

$$N_{\xi_0}(\xi)=\frac{1}{2\sqrt{2}}\ \frac{\xi\sqrt{\sqrt{1+\xi^2}-1}}{1+(\xi^2/\xi_0^2-1)^2\sqrt{1+\xi^2}+\sqrt{2}(\xi^2/\xi_0^2-1)\sqrt{\sqrt{1+\xi^2}+1}}. \tag{6.2}$$

This function of ξ is expanded around $\xi=0$, leading to

$$N_{\xi_0}(\xi)=1-\left(\frac{4}{\xi_0^4}-\frac{3}{\xi_0^2}-\frac{1}{16}\right)\xi^2+O(\xi^4), \tag{6.3}$$

which can be used to show that $N_{\xi_0}(\xi)$ is strictly decreasing for $\xi_0\leqslant\xi_{0c}$, with $\xi_{0c}=2\sqrt{2(\sqrt{10}-3)}\approx 1.1394$. When $\xi_0>\xi_{0c}$, a maximum appears at ξ_m, with $\lim_{\xi_0\to\xi_{0c}}\xi_m=0$ and $\lim_{\xi_0\to\infty}\xi_m=\xi_0$. Also, we infer from Eqs. (6.2) and (6.3) that, when $\xi_0\ll 1$, $N_{\xi_0}(\xi)$ can be approximated by a distinct power law, according to the value of ξ [the $O(\xi^4)$ terms do not add any contribution]. That is, $N_{\xi_0}\approx 1$ when $\xi\ll\xi_0^2$, $N_{\xi_0}\approx\xi_0^4\xi^{-2}/4$ when $\xi_0^2\ll\xi\ll 1$, and $N_{\xi_0}\approx\xi_0^4\xi^{-7/2}/2\sqrt{2}$ when $\xi\gg 1$. In this case, two transition regions can be further detected around $\xi\approx\xi_0^2$ and $\xi\approx 1$.

In our simulations, $\xi_0>0.638$ ($\xi_0^2>0.407$). Therefore we distinguish three regions in the frequency power spectrum.

(1) A plateau corresponding to the low-frequency limit of Eq. (5.2) ($N_{\xi_0}\approx 1$),

$$\lim_{\omega\to 0}|\hat{h}_k(\omega)|^2\ \Big/\ \Theta=\frac{2\rho k\nu\quad k_BT}{\pi^2\ \ (\epsilon k^4)^2 L}, \tag{6.4}$$

which explicitly shows a dependence on the bending stiffness ϵ [55]. Low-frequency excitations are thus controlled by elastic forces and viscous effects. In Fig. 5 this region spans a frequency interval of about two orders of magnitude for the highest wave number, up to where ω approaches the pole of the response function Γ.

(2) A transition region. Notice that the maximum appears in this region only when $\xi_0>\xi_{0c}\approx 1.1394$, which is not the case here. The maximum would, however, appear at higher wave numbers, according to the expression $\xi_0=\sqrt{\epsilon k/2\rho\nu^2}$, showing that ξ_0 is an increasing function of k. This behavior is opposite to that observed for interfaces driven by surface tension, where $\xi_0=\sqrt{\sigma/2\rho\nu^2 k}$ and ξ_0 is thus decreasing with k [51,52].

(3)The high-frequency region, expected from Eq. (5.2) to represent a $\omega^{-7/2}$ decay ($N_{\xi_0}\approx\xi_0^4\xi^{-7/2}/2\sqrt{2}$), independent of either the bending rigidity or the surface tension of the interface, according to

$$\lim_{\omega\to\infty}|\hat{h}_k(\omega)|^2/\Theta=\frac{\sqrt{2\nu}\,k^2\,k_BT}{8\pi^2 L\,\rho}\,\omega^{-7/2}. \tag{6.5}$$

The relative amplitude of this segment of the power spectrum is thus determined by viscosity effects alone.

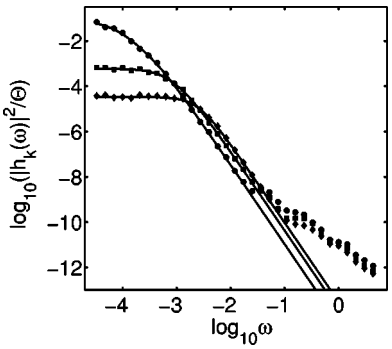

FIG. 5. Frequency power spectrum for a fluctuating interface of size $L=64$, whose time evolution was monitored for 2^{20} time steps. Experimental data for wave numbers $k=2\pi/L, 4\pi/L$ and $6\pi/L$ are reported as filled circles, squares, and diamonds, respectively. The solid lines represent the theoretical predictions from Eq. (5.2), showing that the agreement spans about three orders of magnitude.

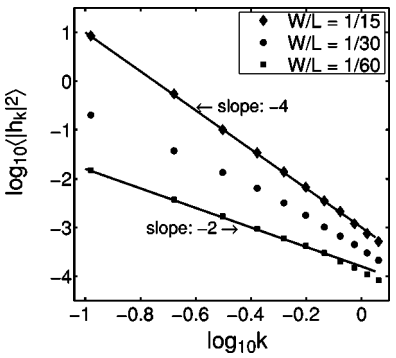

FIG. 6. Power spectra of fluctuating membranes of size $L=60$ lattice units and different bending stiffnesses. The interface width/length ratio W/L ranges from 1/60 to 1/15. When $W/L>1/20$ the purely elastic functional dependence of the power spectrum (with slope of -4 in a log-log plot) is recovered.

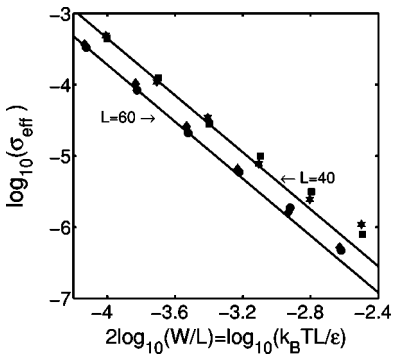

FIG. 7. Effective surface tension obtained from the power spectra of the simulations of fluctuating membranes. Computational boxes with $L=40$ and 60 and different temperatures and bending rigidities were considered. We show a log-log plot of the data for $\sigma_{\rm eff}$ versus $k_BTL/\epsilon=W^2/L^2$.

The experimental results reproduced in Fig. 5 agree with the theoretical predictions, here drawn as solid lines, over a range of about three orders of magnitude, including part of the high-frequency region. The discrepancy with the theory at the highest frequencies is of unknown origin. It may be related to the low signal-to-noise ratio at the highest frequencies, or possibly some other artifact of the discrete Fourier transform.

Since the theoretical prediction (5.2) is confirmed by our numerical results at all but the highest frequencies, the subsequent conclusions, Eqs. (5.8) and (5.10), describe the average wave number power spectrum and the functional dependence of the interface width on the linear dimension of the box. In particular, from Eq. (5.10) we estimate that $W/L\approx 1/16$ for the case just discussed.

B. Effective surface tension

More simulations were performed to verify the agreement with the theoretically predictable wave number power spectrum. Different temperatures, lattice sizes, and bending rigidities were prescribed for the system. In Fig. 6 we report a study of equilibrium power spectra for a lattice of size $L=60$ and bending modulus ϵ ranging from 0.0032 to 0.512. With this set of parameters the ratio W/L spans an interval from 1/6 to 1/60. We notice a very good agreement with Eq. (5.8) when $W/L>1/20$, but for smaller ratios the relation describing the steady state power spectrum is approximated by

$$\langle|h_k|^2\rangle=\frac{k_BT}{(\sigma_{\rm eff}k^2+\epsilon k^4)L}, \tag{6.6}$$

showing the presence of an effective surface tension $\sigma_{\rm eff}$. By considering the small-k limit of Eq. (6.6) when $W/L<1/20$, we measured $\sigma_{\rm eff}$ for different points in the three-dimensional ϵ-L-T space. The following empirical scaling law resulted from our simulations:

$$\sigma_{\rm eff}=\frac{1}{L^2}\mathcal{D}[(W/L)^2]=\frac{1}{L^2}\mathcal{D}(TL/\epsilon), \tag{6.7}$$

where $\mathcal{D}$ is a scaling function. Figure 7 shows a log-log plot of the measured values of $\sigma_{\rm eff}$ versus $(W/L)^2$. Approximately, $\sigma_{\rm eff}$ decays as a power law for increasing values of W/L, namely, $\mathcal{D}(TL/\epsilon)\propto(TL/\epsilon)^{-2}$; also, when $W/L>1/20$ it essentially vanishes and purely elastic dynamics takes place.

In order to discuss the origin of Eq. (6.7), we investigate here the scaling properties of the ratio $\ddot{\gamma}/\gamma$, the crucial factor in the perturbation (3.16) of the Boltzmann equation. For a boundary of the form $h(x)$, the derivative with respect to the arclength s can be expressed in terms of x as

$$\frac{d}{ds}=\frac{1}{\sqrt{1+h'(x)^2}}\frac{d}{dx}, \tag{6.8}$$

where the prime stands for d/dx. From the expression for the curvature,

$$\gamma(x)=\frac{h''(x)}{(1+h'^2)^{3/2}}, \tag{6.9}$$

one obtains

$$\frac{\ddot{\gamma}}{\gamma}=\frac{h^{(4)}}{h''(1+h'^2)}-10\frac{h'h'''}{(1+h'^2)^2}-3\frac{(1-5h'^2)h''^2}{(1+h'^2)^3}. \tag{6.10}$$

In the case of sinusoidal bending waves and fluctuating interfaces with horizontal periodicity as a boundary condition, the profile $h(x)$ satisfies [56]

$$h^{(n)}(x)=\frac{W}{L^n}\mathcal{S}_n(2\pi x/L), \tag{6.11}$$

where $h^{(n)}(x)$ is the nth derivative of $h(x)$ and $\mathcal{S}_n$ is periodic in x with period L. By replacing Eq. (6.11) in Eq. (6.10), we find the following scaling relation for the dynamical factor:

$$\frac{\ddot{\gamma}}{\gamma}=\frac{1}{L^2}\mathcal{G}_{th}[(W/L)^2,x/L], \tag{6.12}$$

where $\mathcal{G}_{th}$ is the theoretical scaling function.

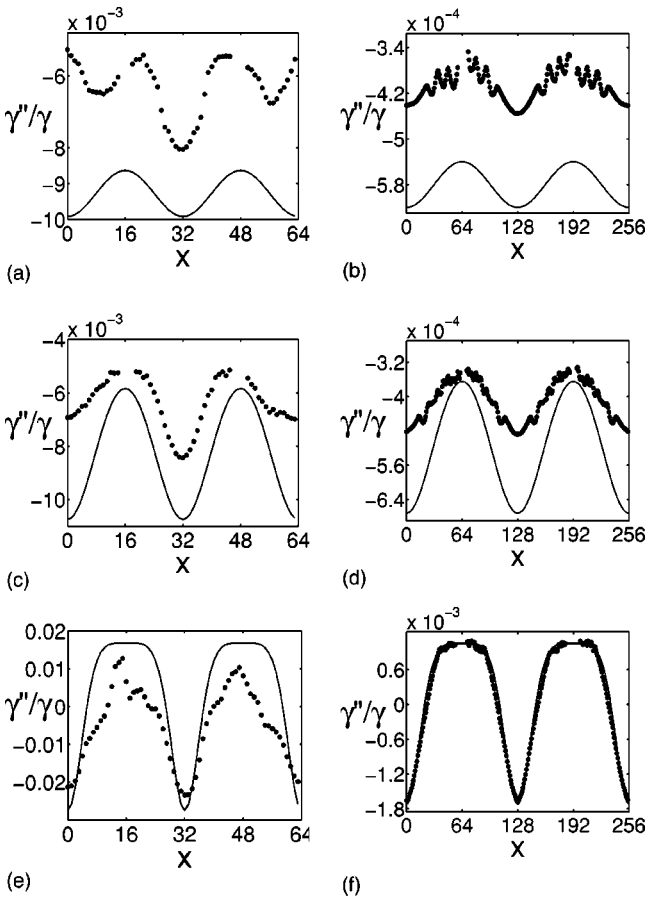

FIG. 8. Measured values of the ratio $\ddot{\gamma}/\gamma$ are plotted as filled circles for static sinusoidal interfaces with wavelengths L of 64 and 256 lattice units and widths W ranging from 1/64 to 1/8 of the wavelengths. Solid lines represent the analytical results for the continuum limit obtained from Eq. (6.10). When $W/L<1/32$, the measured values appear to be shifted with respect to the theoretical ones. This introduces an effective surface tension for almost flat surfaces that scales as a function $\mathcal{D}$ of W and L: $\sigma_{\mathrm{eff}}=\mathcal{D}[(W/L)^2]/L^2$.

After initializing the system with different sinusoidal waves, we measured the ratio $\ddot{\gamma}/\gamma$ for $L=64$ and 256 lattice units and amplitudes ranging from 1/64 to 1/8 of the wavelengths. In Fig. 8 we report the results of such measurements as a function of x. From the figure the experimental behavior of $\ddot{\gamma}/\gamma$ presents the scaling

$$\left(\frac{\ddot{\gamma}}{\gamma}\right)_{ex}=\frac{1}{L^2}\{\mathcal{G}_{ex}[(W/L)^2,x/L]+\mathcal{D}[(W/L)^2]\}, \quad (6.13)$$

where $\mathcal{G}_{ex}$ approaches $\mathcal{G}_{th}$ for large computational boxes (high resolution):

$$\lim_{L\to\infty}\mathcal{G}_{ex}[(W/L)^2,x/L]=\mathcal{G}_{th}[(W/L)^2,x/L]. \quad (6.14)$$

The most notable feature in Eq. (6.13) is the presence of the additional constant term $\mathcal{D}[(W/L)^2]/L^2$. It is responsible for the introduction in our model of an effective surface tension, as it causes S in Eq. (3.16) to be a nonvanishing number.

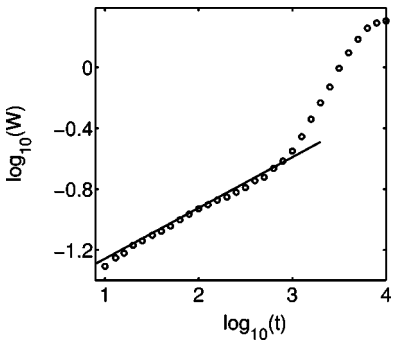

FIG. 9. Log-log plot of the time evolution (circles) of the mean width of an interface with size $L=64$, starting from flatness at time $t=0$, and monitored for an interval of time equal to about twice the crossover time (5.20). The solid line represents the theoretical scaling law $W\propto t^{1/3}$ predicted for the effective surface tension σ_{eff}. The sudden change in slope around $t\approx 10^3$ corresponds to the onset of purely elastic dynamics.

C. Nonequilibrium roughening

As shown in Sec. V B, at large times the average interface width reaches its equilibrium value given by Eq. (5.10). Before reaching the stationary state, though, the interface growth is described by the power law (5.19). In this section we present the results of the simulation of nonequilibrium growing interfaces and compare them with the theoretical predictions.

After initializing the system as a flat boundary separating two immiscible prethermalized fluids, we monitored the growth of the interface for a period of time approximately equal to twice the crossover time t_c estimated in Eq. (5.20). We repeated the simulation 100 times and averaged the results, in order to obtain the mean quantities that appear in Eqs. (5.10) and (5.19). Such an experiment is reported in Fig. 9, where the solid line represents the expected behavior of the interface growth, taking into account the presence of the effective surface tension. From the figure, the early-time evolution of the interface growth appears to be described by the scaling law $W\propto t^{1/3}$ [52]. Again, we conclude that the membrane is indeed driven by σ_{eff} for very small interface width/length ratios, that is, for almost flat boundaries. In order to bypass the effect of the surface tension and analyze the purely elastic nonequilibrium dynamics, the membrane profile is initialized in such a way that $W/L>1/20$. Under these conditions, the disturbance due to σ_{eff} is negligible (as shown in Sec. VI A). The Fourier components of the interface profile are prescribed as

$$h_k(t_0)=\sqrt{\frac{2k_BT}{\epsilon Lk^4}}\sin[\omega_0(k)t_0],$$

where $t_0=t_c/4$ is the time at which the numerical simulation starts; furthermore, the relative intensities of $h_k(t_0)$ have been chosen so that they agree with the evolution (5.12). We studied the nonequilibrium roughening of such interfaces for an interval of time starting at $t_c/4$ and terminating at approximately $3t_c$, after the equilibrium width is attained. In Fig. 10(a) we report the interface widths for system sizes $L=32$, 48, 64, and 96, rescaled as $W/L^{3/2}$ so as to match the prefactor $\sqrt{k_BT/720\,\epsilon}$ from the anticipated steady state

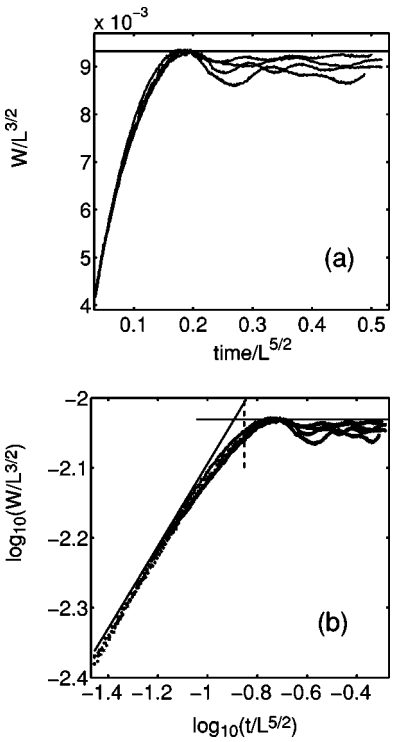

FIG. 10. In (a) we plot the rescaled interface width $W/L^{3/2}$ in lattice units, as a function of the time, scaled to $t/L^{5/2}$ so as to make all the crossover times match the prefactor $\sqrt{\rho/64\,\pi^3\,\epsilon}$ predicted from Eq. (5.20). The computational box sizes are $L=32,48,64$, and 96. The horizontal line represents the steady state width as in Eq. (5.10). In (b) a log-log plot of the same data is given. The dashed line marks the scaled crossover time, while the oblique line represents the theoretical prediction from Eq. (5.19), with an angular coefficient of 3/5. The symbols represent different values of the system size: squares, diamonds, filled circles, and six-pointed stars correspond to $L=32,48,64$, and 96 respectively.

(5.10), drawn in the figure as a solid line. The horizontal coordinate in Fig. 10(a) represents the time t in lattice units, rescaled as $t/L^{5/2}$ so that all the crossover times fall at $\sqrt{\rho/64\,\pi^3\,\epsilon}$, according to Eq. (5.20). In order to evaluate the prefactors above, we used the relations (3.15), (3.17), and (4.5), where the parameters for this experiment were set to $\lambda_B=-1.5$, $E=0.0002$, $\rho=0.5$ and the variance A to 10^{-4}. A log-log plot of the same data is shown in Fig. 10(b). Also, the predicted scaling law (5.19) is represented as a solid line with angular coefficient 3/5. We notice a good agreement between the numerical results and the theoretical predictions, although we were able to investigate the nonequilibrium behavior in a time range of just about one-half the order of magnitude.

VII. CONCLUSIONS

Fluctuating elastic interfaces in fluids have been discussed from different approaches. By means of the fluctuation-dissipation theorem, we presented a theoretical derivation of nonequilibrium interface roughening, described by the scaling law $W^2=L^3\,g(t/L^{5/2})$. This expression predicts that the interface, initially flat, grows as $W\propto t^{3/5}$, and at long times it reaches the equilibrium width $W=\sqrt{k_BT/720\,\epsilon}\,L^{3/2}$. Also, we showed that the correlation function of the fluctuations decays exponentially in the long-time limit, in agreement with the behavior of the correlated forces on the interface, due to the excitations in the bulk [52].

Although the theoretical discussion was necessary for the sake of clarity, this work instead focused on the development of a numerical method simulating the phenomenology of fluctuating membranes. We created a lattice-Boltzmann method. Starting from the description of the membrane dynamics by means of the Landau-Helfrich free energy [1,34], in which the interface geometry appears explicitly in the form of the curvature γ and its derivatives, we translated the macroscopic equation of motion governing the interface evolution into a perturbation of the single-relaxation-time lattice-Boltzmann equation. Such a perturbation depends on γ, so that a crucial point of our model is the localization of the interface and the measurement of its geometric properties. As outlined in Appendix B, we adopted an explicit characterization of the boundary followed by a polynomial mapping, from which we extracted the information about the local curvature.

We tested our method to reproduce the hydrodynamic equilibrium of circular bubbles and the dynamical coupling of the interface with the surrounding fluids in the bending wave dispersion relation. Thermal fluctuations were introduced in the model by adding a random component to the fluid stress tensor [49]. The lattice-Boltzmann equation was thus generalized to include a stochastic term [35], whose fluctuations are uncorrelated in space and time. The equilibrium frequency power spectrum of fluctuating elastic interfaces, predicted by the theory and related to the correlation function of the excitations, was confirmed in our numerical simulations. Also, we simulated the nonequilibrium roughening of membranes, monitoring the time evolution of the interface width. Its growth rate was in agreement with the theoretical predictions mentioned above, although we noticed a disturbance due to numerical errors at almost flat surfaces, generating an unwanted effective surface tension. In order to improve the effectiveness of the interface detection process, other, more accurate, techniques for tracking the interface could be considered. For example, using markers in the context of an explicit discretization of the interface [57,58] could further improve the performance of this numerical method.

One of the advantages of our numerical method relies on the fact that γ and $d^2\gamma/ds^2$, the second derivative in the arclength s, are not approximated by their linearized expressions d^2h/dx^2 and d^4h/dx^4 respectively [here $h(x)$ is the boundary profile]. We could thus use our model to study and simulate systems in the nonlinear regime, that is, when the interface is far from being flat and the curvature is a nonlinear function of the interface profile. Another feature of this method is that it has been designed from the outset to describe thin interfaces separating two (or more) fluids, a situation that is difficult to describe in terms of a slowly varying continuous field (order parameter). In future work, we would like to employ this model in the study of fluctuating membranes separated into many distinct components, colliding with each other and immersed in fluids with prescribed or complex fields. Also interesting would be the inclusion of a surfactant species, as in the microemulsion model of Ref. [44].

ACKNOWLEDGMENTS

We thank Tom Chou and Michael Brenner for valuable discussions. We are also indebted to Tony Dinsmore, Peter Sheridan Dodds, and Joshua Weitz for useful comments. We wish to express our gratitude to Dominique d'Humières for his critical reading of the manuscript and for suggesting an explicit form for the frequency power spectrum and the subsequent analysis.

APPENDIX A: FLUID-INTERFACE COUPLING

In the following we review the dynamical coupling between the membrane and the surrounding fluid, generalizing the results to n-dimensional interfaces. The 2D case with a saddle-splay term in the free energy (2.1) is also presented. We shall denote by $\boldsymbol{r}\equiv(x_1,\ldots,x_{n+1})$ the locus of the n-dimensional hypersurface embedded in the $(n+1)$-dimensional space. The hypersurface is parametrized by the n coordinates $u_1,\ldots,u_n$, collectively referred to as u, so that $\boldsymbol{r}\equiv\boldsymbol{r}(u)$. $\boldsymbol{n}(u)$ represents the unit normal to the surface oriented outward and $\boldsymbol{e}_i\equiv\partial\boldsymbol{r}/\partial u_i$ is the tangent vector corresponding to the coordinate u_i. We shall assumes that the hypersurface is well behaved and we are able to choose a parametrization u such that

$$\langle \boldsymbol{e}_i,\boldsymbol{e}_j\rangle=\boldsymbol{e}_i\cdot\boldsymbol{e}_j=\delta_{ij}. \tag{A1}$$

The Weingarten operator, defined as $L(\boldsymbol{e}_i)\equiv\partial\boldsymbol{n}/\partial u_i$, is self-adjoint with respect to Eq. (A1), and the $\boldsymbol{e}_i$'s are chosen to be eigenvectors of L

$$L(\boldsymbol{e}_i)\equiv\frac{\partial\boldsymbol{n}}{\partial u_i}=\gamma_i\boldsymbol{e}_i, \tag{A2}$$

where γ_i is the principal curvature corresponding to $\boldsymbol{e}_i$. In other words, our parametrization u runs along the principal directions of curvature. We shall apply Hamilton's principle [59] to the line integral of the Lagrangian describing the interface dynamics,

$$\mathcal{I}_{id}=\int\int\left(\frac{\rho}{2}\dot{\boldsymbol{r}}^2-\frac{\epsilon}{2}H^2-\sigma\right)dSdt, \tag{A3}$$

where ρ is the density of the hypersurface, ϵ is the bending rigidity, $H=\Sigma_i\gamma_i$ is the mean curvature and σ is the surface tension. $dS=du_1\ldots du_n$ is the volume element for the given parametrization. By means of Eqs. (A1) and (A2) one can verify that

$$\frac{\partial^2\boldsymbol{r}}{\partial u_i^2}=\frac{\partial\boldsymbol{e}_i}{\partial u_i}=-\gamma_i\boldsymbol{n}, \tag{A4}$$

so that Eq. (A3) is recast as

$$\mathcal{I}_{id}=\int\int\left[\frac{\rho}{2}\dot{\boldsymbol{r}}^2-\frac{\epsilon}{2}(\nabla_u^2\boldsymbol{r})^2-\sigma\prod_i|\partial_{u_i}\boldsymbol{r}|\right]dSdt \tag{A5}$$

where

$$\dot{\boldsymbol{r}}=\frac{d\boldsymbol{r}}{dt},\quad \nabla_u^2\boldsymbol{r}=\sum_i\frac{\partial^2\boldsymbol{r}}{\partial u_i^2},\quad |\partial_{u_i}\boldsymbol{r}|=1.$$

A variation of Eq. (A3) reads

$$\delta\mathcal{I}_{id}=\int\int\left(\rho\dot{\boldsymbol{r}}\cdot\frac{d}{dt}\delta\boldsymbol{r}-\epsilon\nabla_u^2\boldsymbol{r}\cdot\nabla_u^2\delta\boldsymbol{r}-\sigma\sum_j\frac{\partial\boldsymbol{r}}{\partial u_i}\cdot\frac{\partial}{\partial u_i}\delta\boldsymbol{r}\right)dSdt. \tag{A6}$$

Upon integration by parts, the boundary terms vanish as we study closed surfaces or impose periodic boundary conditions and all of the derivatives involved are supposed to be smooth functions of the coordinates u. Therefore, by applying Hamilton's principle, including a term for an external force $\boldsymbol{F}_{ext}$,

$$\delta\mathcal{I}=\int\int[-\rho\ddot{\boldsymbol{r}}-\epsilon(\nabla_u^2)^2\boldsymbol{r}+\sigma\nabla_u^2\boldsymbol{r}]\cdot\delta\boldsymbol{r}dSdt+\int\boldsymbol{F}_{ext}\cdot\delta\boldsymbol{r}dt=0, \tag{A7}$$

one retrieves the following equation of motion:

$$\boldsymbol{F}_{ext}=-\sigma\nabla_u^2\boldsymbol{r}+\epsilon(\nabla_u^2)^2\boldsymbol{r}+\rho\ddot{\boldsymbol{r}}. \tag{A8}$$

If $\boldsymbol{F}_{ext}$ is the pressure, it is directed along the normal to the surface, that is, $\boldsymbol{F}_{ext}=F\boldsymbol{n}$. By noticing that Eqs. (A4) and (A2) lead to

$$(\nabla_u^2)^2\boldsymbol{r}=(\nabla_u^2)(-H\boldsymbol{n})=-\left(\nabla_u^2H-H\sum_i\gamma_i^2\right)\boldsymbol{n}+\sum_i\left(2\gamma_i\frac{\partial H}{\partial u_i}+H\frac{\partial\gamma_i}{\partial u_i}\right)\boldsymbol{e}_i \tag{A9}$$

and by projecting $\ddot{\boldsymbol{r}}$ along the normal and tangential components, Eq. (A8) can be separated as

$$F-\rho\ddot{\boldsymbol{r}}\cdot\boldsymbol{n}=\sigma H-\epsilon\nabla^2H+\epsilon H\sum_i\gamma_i^2, \tag{A10}$$

$$\rho\ddot{\boldsymbol{r}}\cdot\boldsymbol{e}_i/\epsilon=2\gamma_i\partial H/\partial u_i+H\,\partial\gamma_i/\partial u_i,\quad i=1,\ldots n, \tag{A11}$$

where we have dropped the subscript u in the Laplacian as it is invariant for any isometric reparametrization. The main result of this Appendix is that the dynamical coupling between the interface and the fluid in the lattice-Boltzmann method is provided by Eq. (A10). Since the macroscopic motion of the membrane is extremely slow in terms of lattice units, of $O(10^3)$ time steps, the second term in the left-hand side of Eq. (A10) can be neglected for our purposes and we shall regard

$$F=\sigma H-\epsilon\nabla^2H+\epsilon H\sum_i\gamma_i^2 \tag{A12}$$

as a quasistationary equilibrium between the interface configuration and the surrounding fluid pressure. Similarly it can be shown that the dynamical coupling for a 2D interface, including as in Eq. (2.1) a saddle-splay correction to Eq. (A3), is given by

$$F=\sigma H-\epsilon\nabla^2 H+\epsilon H(H^2-2K)$$
$$+\overline{\epsilon}(HK-\partial^2\gamma_1/\partial u_2^2-\partial^2\gamma_2/\partial u_1^2), \qquad \text{(A13)}$$

where $K=\gamma_1\gamma_2$ is the Gaussian curvature. Equation (A13) should be used in simulating 2D membranes with this lattice-Boltzmann method, when changes in the interface genus are taken into account.

APPENDIX B: EVALUATION OF THE CURVATURE

In this appendix we include a description of the algorithm used in this work to measure the geometric properties of the interface. The procedure is schematically divided into three steps: localization of the interface, polynomial approximation, and evaluation of the local curvature.

As mentioned in Sec. III, the populations corresponding to two immiscible fluids are distinguished from each other by splitting the occupation numbers $n_i(\mathbf{x},t)$ at a given lattice site into a ''red'' part $r_i(\mathbf{x},t)$ and a ''blue'' part $b_i(\mathbf{x},t)$ of the distribution function, as in Eq. (3.8). By defining the color field as

$$\Phi(\mathbf{x},t)=\sum_i\,[r_i(\mathbf{x},t)-b_i(\mathbf{x},t)], \qquad \text{(B1)}$$

one can visualize the binary fluid as a 2D surface where its lowest regions correspond to the physical presence of the blue fluid and the flat ''highlands'' to the areas occupied by the red fluid. The interface, in this picture, is represented by the steep slopes. One can define the boundary $\mathcal{B}$ between the two fluids as the set of lattice sites whose color field absolute value is smaller than a fraction α (<1) of the fluid density ρ, that is,

$$\mathcal{B}\equiv\{\mathbf{x}:|\Phi(\mathbf{x},t)|<\alpha\rho\}. \qquad \text{(B2)}$$

In our simulations, due to the small thickness of the interface, α might be chosen to be a value between 0.5 and 0.9 with no substantial changes in $\mathcal{B}$. Another parameter used in the description of the interface is the color gradient $\mathbf{f}$, defined as

$$\mathbf{f}(\mathbf{x},t)=\sum_i\,\mathbf{c}_i\sum_j\,[r_j(\mathbf{x}+\mathbf{c}_i,t)-b_j(\mathbf{x}+\mathbf{c}_i,t)]. \qquad \text{(B3)}$$

From its definition $\mathbf{f}$ appears to be, in the lattice approximation, perpendicular to the interface. The vector $\mathbf{n}\equiv\mathbf{f}/|\mathbf{f}|$ will be used here as the unit normal to the interface.

After localizing the interface, in order to measure its geometrical properties at a certain lattice site $\mathbf{x}_0$ in $\mathcal{B}$, we replace a neighborhood of $\mathbf{x}_0$ with the polynomial resulting from a least-squares fit, as described below. The neighborhood of a given boundary point (in the present case $\mathbf{x}_0$) is constituted by contiguous lattice sites in $\mathcal{B}$ and is chosen so that the following two conditions are met: (1) The normals at the points furthest from $\mathbf{x}_0$ make an angle of at most $\pi/4$ with the normal at $\mathbf{x}_0$; (2) All the boundary points in the neighborhood lie within a distance of 30 lattice units from $\mathbf{x}_0$ (about 10 times the interface width) or half the linear size of the computational box, whichever is smaller.

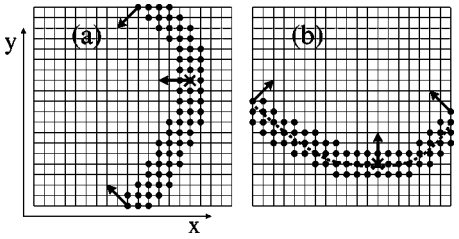

FIG. 11. Filled circles represent an interface neighborhood of a given lattice site $\mathbf{x}_0$ on the boundary (marked by a cross). An arrow indicates the direction of the normal $\mathbf{n}$ to the interface at the corresponding lattice site. The whole set of points in (a) is rotated clockwise by the angle $\vartheta=\arccos(\mathbf{n}\cdot\hat{\mathbf{x}})$ so as to align $\mathbf{n}$ with the y-axis (b). A least-squares fit of the interface can thus be realized by the single-valued polynomial $y=\Sigma_{i=0}^{5}a_i x^i/i!$, here drawn as a dashed line.

In Fig. 11 we present the two-step process. The filled circles represent the lattice sites belonging to the boundary in a neighborhood of the point $\mathbf{x}_0$ (marked by a cross); arrows are magnified representations of the normals at the corresponding lattice sites. As shown in Fig. 11(b), calculations are simplified by rotating the whole set of points clockwise by the angle $\vartheta=\arccos(\mathbf{n}\cdot\mathbf{i})$, where $\mathbf{i}$ is a unit vector directed along the positive x-axis. In this way, we can fit the subset of $\mathcal{B}$ by a single-valued polynomial in x: $y=\Sigma_{i=0}^{N}a_i x^i/i!$, where $x=0$ corresponds to the horizontal coordinate of $\mathbf{x}_0$. It is convenient to choose $N\geqslant 4$, because derivatives up to the fourth order are involved in the evaluation of $\ddot{\gamma}$, the second derivative in the arclength of the curvature. In practice, we let $N=5$, as the accuracy of our method does not improve for larger values of N.

Once the coefficients a_i are estimated, we calculate γ and $\ddot{\gamma}/\gamma$ by replacing $h(x)$ in Eqs. (6.9) and (6.10) with $y=\Sigma a_i x^i/i!$ and setting x to vanish. In other words, a_n substitutes for $h^{(n)}$ in Eqs. (6.9) and (6.10). Also, it is evident from these equations that $\ddot{\gamma}/\gamma$ is an ill-defined function when $\gamma=0$ or, equivalently, $h''=0$. We set the term $\ddot{\gamma}/\gamma$ to vanish in such cases. The dynamical term $\gamma^2(\mathbf{x},t)-\ddot{\gamma}(\mathbf{x},t)/\gamma(\mathbf{x},t)$, appearing in the perturbation (3.16) is thus evaluated by repeating the above procedure for each lattice site $\mathbf{x}$ in $\mathcal{B}$.

[1] L. D. Landau and E. M. Lifshitz, *Theory of Elasticity*, Vol. 7 of *Course of Thoretical Physics*, 3rd ed. (Butterworth Heinemann, Oxford, 1986).

[2] F. Brochard and J. F. Lennon, J. Phys. (France) **36**, 1035 (1975).

[3] J. A. Aronovitz and T. C. Lubensky, Phys. Rev. Lett. **60**, 2634 (1988).

[4] T. Powers and P. Nelson, J. Phys. II **5**, 1671 (1995).

[5] G. Gompper and D. M. Kroll, J. Phys.: Condens. Matter **9**, 8795 (1997).

[6] M. C. Diamantini, H. Kleinert, and C. A. Trugenberge, e-print cond-mat/9903021.

[7] S. Ramanujan and C. Pozrikidis, J. Fluid Mech. **361**, 117 (1998).

[8] W. T. Góźdź and G. Gompper, Phys. Rev. Lett. **80**, 4213 (1998).
[9] Y. Navot, Phys. Fluids **10**, 1819 (1998).
[10] C. D. Eggleton and A. S. Popel, Phys. Fluids **10**, 1833 (1998).
[11] G. Gompper and D. M. Kroll, Phys. Rev. Lett. **81**, 2284 (1998).
[12] W. T. Góźdź and G. Gompper, Phys. Rev. E **59**, 4305 (1999).
[13] A. Elgsaeter, B. T. Stokke, A. Mikkelsen, and D. Branton, Science **234**, 1217 (1986).
[14] C. F. Schmidt *et al.*, Science **259**, 952 (1993).
[15] T. Hwa, E. Kokufuta, and T. Tanaka, Phys. Rev. A **44**, R2235 (1991).
[16] X. Wen *et al.*, Nature (London) **355**, 426 (1992).
[17] Y. Kantor, M. Kardar, and D. R. Nelson, Phys. Rev. Lett. **57**, 791 (1986).
[18] Y. Kantor, M. Kardar, and D. R. Nelson, Phys. Rev. A **35**, 3056 (1987).
[19] M. Paczuski, M. Kardar, and D. R. Nelson, Phys. Rev. Lett. **60**, 2638 (1988).
[20] F. David and E. Guitter, Europhys. Lett. **5**, 709 (1988).
[21] E. Guitter, F. David, S. Leibler, and L. Peliti, J. Phys. (France) **50**, 1787 (1989).
[22] D. C. Morse and S. T. Milner, Europhys. Lett. **26**, 565 (1994).
[23] D. C. Morse and S. T. Milner, Phys. Rev. E **52**, 5918 (1995).
[24] D. C. Morse, Phys. Rev. E **50**, R2423 (1994).
[25] S. A. Safran, *Statistical Thermodynamics of Surfaces, Interfaces and Membranes* (Addison-Wesley, Reading, MA, 1994).
[26] *Structure and Dynamics of Membranes, Handbook of Biological Physics Vol. 1*, edited by R. Lipowsky and E. Sackmann (Elsevier, Amsterdam, 1995).
[27] *Statistical Mechanics of Membranes and Surfaces*, edited by D. Nelson, T. Piran, and S. Weinberg (World Scientific, Singapore, 1989).
[28] F. David, *Two Dimensional Quantum Gravity and Random Surfaces*, No. 8 of *Jerusalem Winter School for Theoretical Physics*, edited by D. J. Gross, T. Piran, and S. Weinberg (World Scientific, Singapore, 1992).
[29] M. J. Bowick and A. Travesset, e-print cond-mat/0002038.
[30] A. D. Dinsmore, D. T. Wong, P. Nelson, and A. G. Yodh, Phys. Rev. Lett. **80**, 409 (1998).
[31] R. Goetz, G. Gompper, and R. Lipowsky, Phys. Rev. Lett. **82**, 221 (1999).
[32] G. Gonnella, E. Orlandini, and J. M. Yeomans, Int. J. Mod. Phys. C **8**, 783 (1997).
[33] O. Theissen, G. Gompper, and D. M. Kroll, Europhys. Lett. **42**, 419 (1998).
[34] W. Helfrich, Z. Naturforsch. C **28**, 693 (1973).
[35] A. J. C. Ladd, J. Fluid Mech. **271**, 285 (1994).
[36] A. J. C. Ladd, J. Fluid Mech. **271**, 311 (1994).
[37] D. H. Rothman and S. Zaleski, *Lattice-Gas Cellular Automata* (Cambridge University Press, Cambridge, England, 1997).
[38] S. S. Chern, Ann. Math. **45**, 747 (1944).
[39] S. F. Edwards and K. F. Freed, J. Chem. Phys. **61**, 1189 (1974).
[40] R. A. Harris and J. E. Hearst, J. Chem. Phys. **44**, 2595 (1966).
[41] S. Chen and G. D. Doolen, Annu. Rev. Fluid Mech. **30**, 329 (1998).
[42] A. K. Gunstensen, D. H. Rothman, S. Zaleski, and G. Zanetti, Phys. Rev. A **43**, 4320 (1991).
[43] J. S. Rowlinson and B. Widom, *Molecular Theory of Capillarity* (Clarendon Press, Oxford, 1982).
[44] B. M. Boghosian, P. V. Coveney, and A. N. Emerton, Proc. R. Soc. London, Ser. A **452**, 1221 (1996).
[45] U. Frisch *et al.*, Complex Syst. **1**, 649 (1997).
[46] F. Higuera, S. Succi, and R. Benzi, Europhys. Lett. **9**, 345 (1989).
[47] Y. Qian, D. d'Humiéres, and P. Lallemand, Europhys. Lett. **17**, 479 (1992).
[48] H. Chen, S. Chen, and W. H. Matthaeus, Phys. Rev. A **45**, R5339 (1992).
[49] L. D. Landau and E. M. Lifshitz, *Fluid Mechanics*, Vol. 6 of *Course of Thoretical Physics*, 2nd ed. (Butterworth Heinemann, Oxford, 1995).
[50] P. M. Morse and K. U. Ingard, *Theoretical Acoustics*, 1st ed. (Princeton University Press, Princeton, NJ, 1986).
[51] E. G. Flekkøy and D. H. Rothman, Phys. Rev. Lett. **75**, 260 (1995).
[52] E. G. Flekkøy and D. H. Rothman, Phys. Rev. E **53**, 1622 (1996).
[53] J. C. Herpin and J. Meunier, J. Phys. (France) **35**, 847 (1974).
[54] I. S. Gradshteyn and I. M. Ryzhik, in *Table of Integrals, Series, and Products*, 5th ed., edited by A. Jeffrey (Academic Press, New York, 1980), p. 484, Eq. 3.823.
[55] In the case of a nonvanishing surface tension σ, the denominator of Eq. (6.4) changes according to $\epsilon k^4 \rightarrow \epsilon k^4 + \sigma k^2$.
[56] D. Stelitano, Ph.D. dissertation, Massachusetts Institute of Technology, Department of Physics, 2000 (unpublished).
[57] S. Popinet and S. Zaleski, Int. J. Numer. Methods Fluids **30**, 775 (1999).
[58] R. Scardovelli and S. Zaleski, Annu. Rev. Fluid Mech. **31**, 567 (1999).
[59] H. Goldstein, *Classical Mechanics*, 1st ed. (Addison-Wesley, Reading, MA, 1965).